ACS OMEGA

http://pubs.acs.org/journal/acsodf
Article

Invagination of Giant Unilamellar Vesicles upon Membrane Mixing with Native Vesicles

Published as part of ACS Omega special issue "Celebrating the 25th Anniversary of the Chemical Research Society of India".

Garvita Dhanawat, Manorama Dey, Anirudh Singh, and Nagma Parveen*

Cite This: ACS Omega 2024, 9, 46615−46626
Read Online

ABSTRACT: We demonstrate rapid membrane mixing between GUVs of pure lipid compositions and membrane vesicles (MVs) isolated from the plasma membrane of Vero cells, resulting in the transfer of native lipids and proteins to the GUVs. The steps involved in the membrane mixing are docking followed by membrane fusion. We show that positively charged lipids of the GUVs are essential for the docking, and the native membrane components of MVs drive the fusion. The interleaflet and lateral asymmetry and a change in the membrane tension upon the membrane mixing trigger membrane invagination. We detected outward and inward invagination sites at the rim of the GUVs within 10−40 min of the membrane mixing. The extent of the invaginations depends on the cholesterol and sphingomyelin (SM) contents in the GUVs. Cholesterol content above a critical concentration disfavors membrane invaginations, and the SM lipid is an essential molecular factor for membrane invagination.

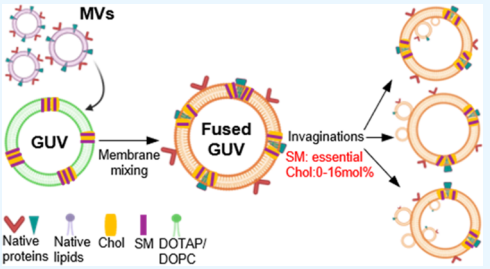

INTRODUCTION

GUVs were first formulated by Reeves and Dowben in 1969 from pure phospholipids using the swelling method.[1] Their controllable lipid composition, rapid formulation, and micrometer size, which are ideal for imaging with optical microscopy techniques, make them an attractive model system for studying dynamic membrane processes. Over the years, two major topics of GUV research have been membrane fusion and invagination (curvature formation). These two processes are interconnected and are reported to be critical in protein uptake,[2] infection propagation,[3] inter- and intracellular transport,[4,5] etc.

Membrane fusion is associated with the attachment of fusogenic peptides, proteins, viruses, or functionalized nanoparticles to the outer membrane of GUVs.[6−8] Membrane invagination events, reported as membrane curvature, bending, budding, and tubulation, can be induced by osmotic stress, adhesion of ions, molecules, or particles on either side of the bilayer.[9,10] Early on Baumgart et al. and Bacia et al. have shown that GUVs with macroscopic phase separation (having both liquid-ordered and disordered phases) can spontaneously curve the membrane at the phase boundary.[11,12]

Other than phase separation, attachment or fusion of proteins and peptides on GUVs is also reported to trigger membrane deformation/curvature formation. For example, Nomura et al. reported that fusogenic peptides cause certain membrane deformations in GUVs, which catalyze fusion between adjacent GUVs.[13] Charged peptides are reported to form pores in GUV bilayers, inducing membrane buds.[14] Here, the coexistence of liquid-ordered and liquid-disordered phases and the presence of cholesterol influence the number and type of surface budding. Adhesion or specific binding of bolapeptides, nanoparticles, non-enveloped viruses, or proteins to GUVs causes inward invagination, forming inward buds and tubules.[15,16] Even GUVs with a relatively complex composition experience membrane invagination upon external stimuli, such as osmotic stress. Nair et al. reported that lipopolysaccharides and bacterial lipids in GUVs favor the formation of membrane buds, nanotubes, and other morphologies.[17] These lipids alter the membrane bending rigidity and line tension, making them softer and more easily deformed. The group of Karin Riske has reported lipid-mediated membrane fusion and deformation for a combination of oppositely charged GUVs and LUVs.[18] These GUV studies indicate that lipid composition and added components upon membrane fusion alter membrane morphology and tension, which in turn can induce membrane invagination.

Beyond these fundamental studies, an emerging research area is the reconstitution of native proteins in GUVs to

Received: October 1, 2024
Revised: October 14, 2024
Accepted: October 23, 2024
Published: November 7, 2024

https://doi.org/10.1021/acsomega.4c08971
ACS Omega 2024, 9, 46615−46626

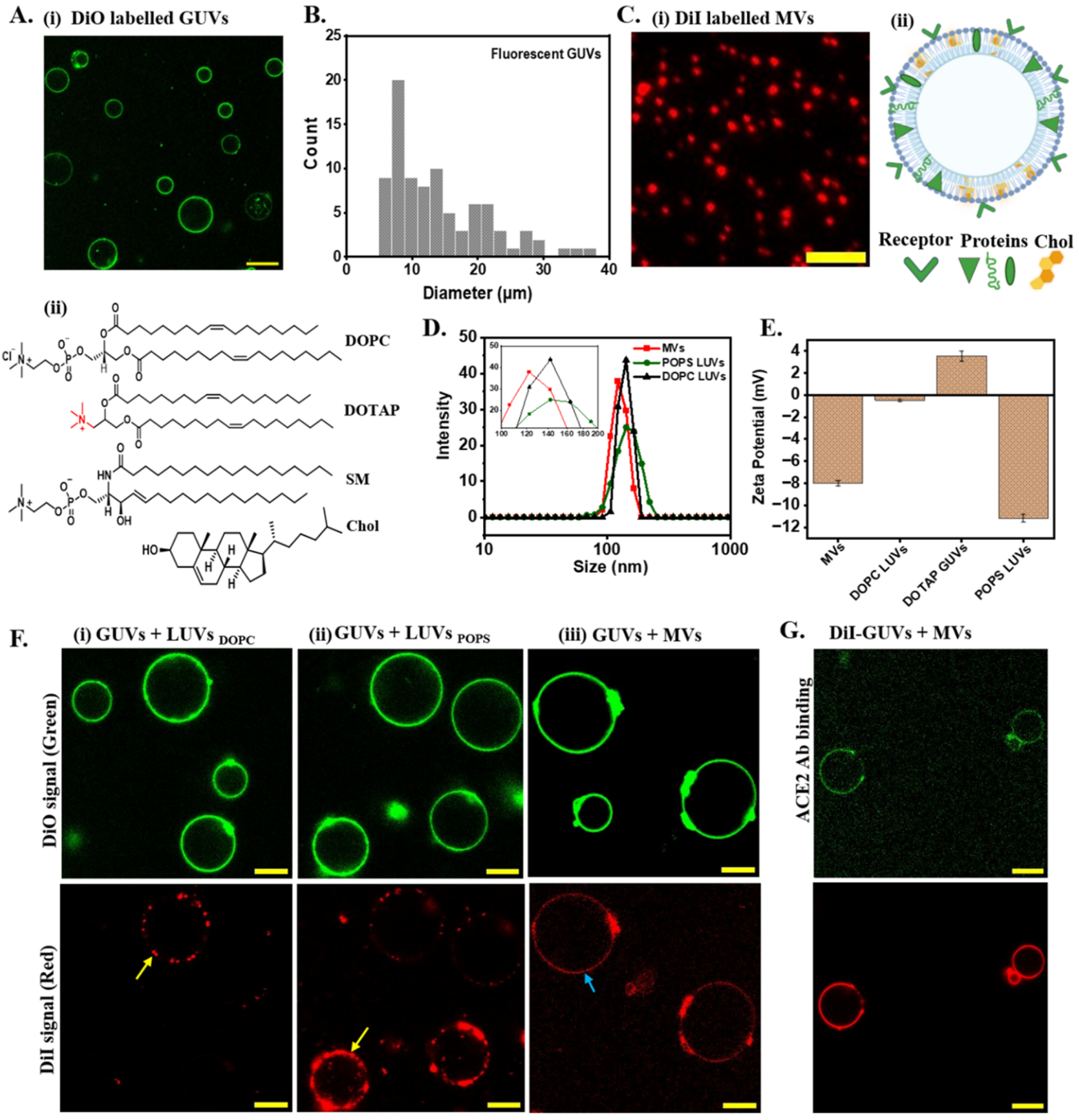

Figure 1. Membrane mixing of GUVs and Vero cell MVs. (A) (i) Confocal image of DiO-labeled GUVs in FITC channel. (ii) Chemical structure of the lipids (DOPC, DOTAP, SM, and cholesterol) used to form positively charged GUVs. (B) Size distribution of GUVs (N = 90) formed by the PVA-gel-assisted method in 10 mM Ca^{2+} buffer. The average size of DiO-labeled GUVs is 14.3 ± 7.4 μm. (C) (i) TIRF micrograph of DiI-labeled MVs on a borosilicate glass surface. (ii) Cartoon representation of single MV carrying native membrane receptors, proteins, and lipids. (D) Distribution of hydrodynamic diameter of MVs, POPS LUVs, and DOPC LUVs. The inset is shown for the clarity of peaks. (E) Bar graphs represent the ζ potential of MVs, LUVs, and GUVs used in experiments. The average and standard deviation (error) of 3 days of measurements are plotted. (F) Confocal images of DiO-labeled GUVs after 10 min incubation with DiI-labeled (i) DOPC LUVs, (ii) POPS LUVs, and (iii) MVs in both green and red channels (yellow arrow indicating docked LUVs and blue arrow indicating membrane mixing by MVs). More micrographs of these systems are shown in Figure S3E in the SI. (G) Confocal images of DiI-labeled GUVs shown in red channel (below) fused with unlabeled MVs, followed by anti-ACE2 antibody binding. Signal of GUVs in the green channel (top) indicates the antibody binding to ACE2. Scale bar: 10 μm, and 5 μm for C(i).

generate artificial cells in bottom-up synthetic biology.[19,20] Different methods, such as osmotic shock and hydrogel methods, are established to form proteo-GUVs.[21,22] However, the detergent-solubilization step used for protein isolation may have an impact on the structure and function of the reconstituted protein. Recently, Schmid et al. have demonstrated a detergent-free method of protein reconstitution in GUVs using cell-derived vesicles, which can fuse with GUVs in

https://doi.org/10.1021/acsomega.4c08971
ACS Omega 2024, 9, 46615−46626

a calcium-dependent manner.[23] This study exploits the membrane fusion phenomenon to generate artificial cells with a functional membrane composition. Such compositional transfer can influence the membrane morphology and tension, triggering membrane invagination.

In this work, we demonstrate membrane mixing between GUVs formulated from ternary/quaternary lipid mixtures and native membrane vesicles isolated from Vero cells. We explored the interactions or molecular factors involved in the mixing with dual-color fluorescence imaging of the GUVs by employing the confocal microscopy technique. The imaging data reveal that the membrane mixing leads to spontaneous curvature formation in the parent GUVs, appearing as inward and outward invagination sites. To the best of our knowledge, membrane invagination upon reconstitution of native membrane lipids and proteins in GUVs has not been previously reported. We examined and discussed the role of cholesterol and sphingomyelin lipids in driving the membrane mixing and affecting the extent of membrane invagination.

RESULTS

We examined the mixing of the membrane between GUVs and membrane vesicles (MVs) isolated from live Vero cells. For this, positively charged GUVs of a quaternary composition were formulated by mixing DOPC, DOTAP, SM (brain sphingomyelin), and cholesterol in a molar ratio of 2:1:2:1 (32:16:32:16 mol %), see Figure 1A. The GUVs were formed with PVA-gel-assisted hydration method which was established earlier by Carlos Marques group[24] and applied by multiple groups.[17,25,26] GUV formation with gels is rapid. Unlike electroformation and hydration methods, it works for a wide range of lipids and at different buffer conditions.

GUVs were formed through the hydration of a lipid film on a PVA-coated surface (see the Methods section and Figure S1A for details). To produce large-sized GUVs, with diameters ranging from 5 to 40 μm (Figure 1B), we utilized a buffer with a relatively high calcium concentration (10 mM). This approach also helped to reduce their aggregation. This is confirmed by capturing bright-field and differential interference contrast (DIC) images of the GUVs without any labels/markers (Figure S1B in the SI). For fluorescence imaging of the GUVs, we used membrane anchoring fluorophores such as DiO (green channel) or DiI (red channel). Majority of the presented images are of GUVs with 4 mol % DiO (details in the Methodssection). We detected a smooth signal along the surface of GUVs representing a homogeneous distribution of the membrane anchoring dye, which in turn is an indicator of liquid-disorder phase of the lipids.[27,28] A similar smooth signal is detected when the GUVs were labeled using Rh-DHPE (Figure S2A-i) and an irregular/uneven distribution of the fluorescent signal can be seen only if SM is replaced by DSPC lipid (details in Figure S2A-ii). This Supporting Information Data confirms that our GUV composition does not exhibit any macroscopic phase separation. The surface charge of the GUVs is characterized by ζ potential measurements (Figure 1E). We found that the ζ potential and thereby the effective surface charge of the GUVs is proportional to DOTAP content in the vesicles (Table S1 in SI). Interestingly, the surface density of DOTAP on the vesicles calculated from the measured ζ potential corresponds to 16 mol % (total) DOTAP (details in the description of Tables S1 and S2). This means that our lipid mixture used is well translated into the lipid bilayer of the formed GUVs. Hence, the PVA-gel-assisted GUV method provides good control of the GUV compositions.

For the generation of MVs, we chemically isolated giant plasma membrane vesicles (GPMVs)[29,30] by introducing N-ethylmaleimide (NEM) to Vero cells (Figure S1C and S1D in the SI). The GPMVs are 2−20 μm in diameter (Figure S1E) and downscaled upon extrusion to form MVs (details in the Methods section). This downsizing is confirmed by the fluorescence images of the vesicles (Figure 1C) and from their measured size distributions before and after extrusion (Figures 1D and S1F). The functionality of the MVs was confirmed by the presence of endogenous ACE2 as detected by Western blotting and antibody binding (Figures S1G and S1H). For control experiments, we formulated large unilamellar vesicles (LUVs) of simple lipid compositions (DOPC with and without POPS, details in the Methods section). These LUVs and MVs are of similar size (∼150 and 120 nm in diameter) as evident from their DLS data, see Figure 1D. The surface charge of MVs and the control LUVs, i.e., DOPC with POPS is comparable (about −8 to −10 mV) and the GUVs are positively charged with a ζ potential of about +3.5 mV (Figure 1E). The ζ potential of MVs is similar to the reported surface charge of membrane blebs which are proteo-liposomes (100−250 nm) protruding from the cell surface upon starvation or chemical induction.[31,32]

We examined the effect of added MVs on the positively charged GUVs by recording dual-color fluorescence images by using confocal microscopy. In control experiments, confocal images were captured upon the addition of LUVs to the GUVs. Representative confocal images of DiO-labeled GUVs (in green channel) and DiI-labeled LUVs or MVs (in red channel) are shown in Figure 1F(i−iii). The red channel signal shows that DOPC LUVs dock on the membranes of GUVs. The docking events are many for POPS LUVs (negatively charged). About 1−7 DOPC LUVs dock per imaging plane of a single GUV (of diameter ≥10 μm), whereas the POPS LUVs are densely docked on the GUVs making it difficult to count their number per GUV. These data are analyzed from z-stack confocal images of the GUVs and signal overlap from the adjacent z-stacks is avoided by choosing the appropriate step size while imaging (details in Methods section). We confirm that DiI labeling does not influence these data because Rh-DHPE labeled LUVs also show a similar docking pattern (Figure S2B).

The fluorescence signal appears to be quite different when MVs are added to the GUVs. The DiI-labeled MV particles are diffused immediately after their addition to surface-adhered GUVs. At the later time points, neither docked MVs nor diffusive MVs were detected (Figure 1F-iii). We observed a smooth signal along the rim of GUVs in the red channel (DiI signal from MVs). About 80% of the imaged GUVs (180 vesicles) show a smooth signal along the membrane rim. This homogeneous signal is not because of the photoleaking or bleed-through of the DiO fluorescence in the red channel because (i) not all DiO-labeled GUVs have signal in the red channel (see the confocal micrograph in Figure 1F-iii) and (ii) DiO-labeled GUVs (without MVs) show a relatively weak photoleaking or bleed-through in the red channel (Figure S3A−C). Also, we recorded bright-field and fluorescence images (red channel) by adding DiI-labeled MVs to the nonlabeled GUVs. Here, a homogeneous signal of DiI along the rim of GUVs was observed (Figure S3D). The lateral mobility of the transferred DiI in the GUVs was examined with

https://doi.org/10.1021/acsomega.4c08971
ACS Omega 2024, 9, 46615−46626

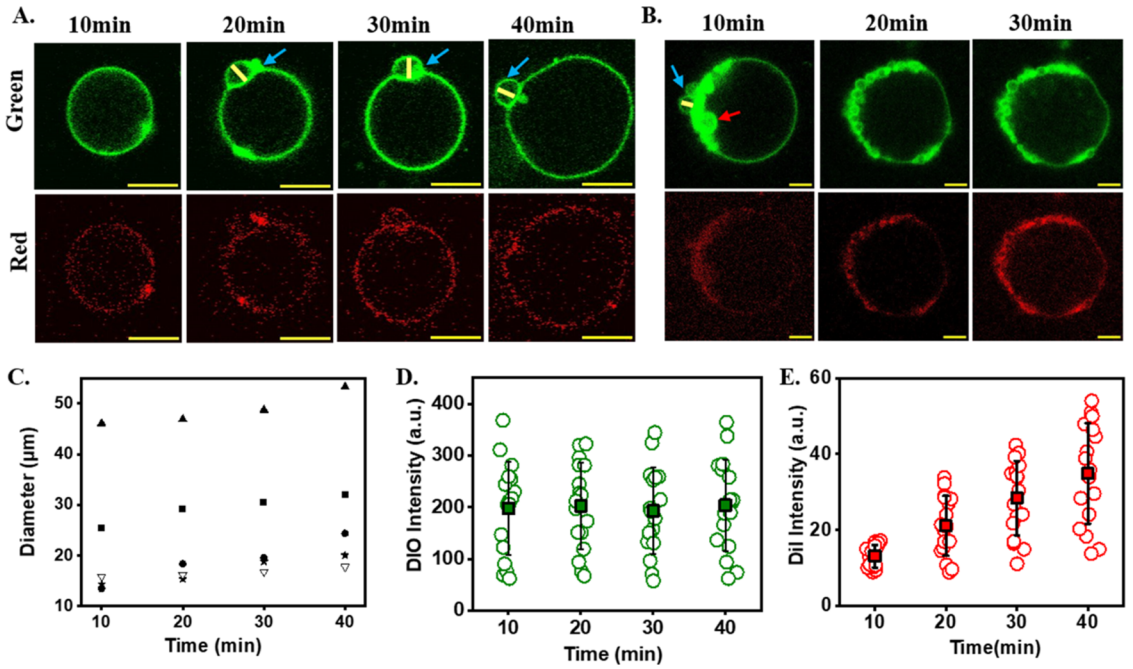

Figure 2. GUV membrane invagination. Time-lapse confocal images of (A) GUV showing single outward invagination and (B) GUV showing multiple invaginations. The GUVs are incubated with MVs for 10 min in the PDMS before recording the image on both channels. Blue and red arrows point outward and inward invaginations, respectively. And yellow line indicates the size of invaginations. (C) Time-dependent scatter plot of GUVs (N = 5) showing an increase in the diameter of GUVs with time. (D) DiO signal (green channel) of GUVs and (E) DiI signal (red channel) of GUVs (N = 20) at different time points of the imaging. Scale bar:10 μm.

fluorescence recovery after photobleaching (FRAP), as shown in the micrographs in Figure S3G. The half-time of recovery ($t_{1/2}$) determined from the FRAP measurements is 15−25 s (Figure S3H and S3I). It is similar to the reported $t_{1/2}$ of NBD-lipid and other lipids used for labeling of GUVs and corresponds to a 2D diffusion coefficient of ∼1−1.5 $\mu m^2/s$ (discussed in SI).[18,33,34] The FRAP data exhibit that the smooth DiI signal detected in our GUV membrane is from laterally mobile molecules of the dye.

With these imaging and FRAP data, we confirm that the DiI fluorophore is transferred from MVs to GUVs upon merging of their lipid membranes. This is possible if the MVs fuse upon docking to the outer membrane of GUVs and the native membrane components are transferred to the bilayer of the GUVs. However, we did not detect docking of MVs on GUVs under our measured conditions presumably due to the fast membrane mixing. Other than the lipid transfer as probed using the lipid anchoring fluorophore (DiI), we examined the transfer of membrane proteins with an immunofluorescence assay. Figure 1G shows a representative immunofluorescence image marking endogenous ACE2 on GUVs after the membrane merges with MVs. About 80% of the imaged GUVs (60 GUVs) show the anti-ACE2 signal, confirming a transfer of the native membrane protein from MVs to GUVs.

Interestingly, we detected the formation of inward and outward membrane invaginations (indicated with red and blue arrows respectively) upon membrane merging (Figure 2A,B). About 50% of the imaged GUVs show membrane invaginations, which are mostly spherical and 1−5 μm (Figure S3F in the SI) in diameter indicated by the yellow line in Figure 2A. A single GUV either contains inward, outward, or both types of invaginations (single or multiple). These invagination sites are specific to the GUVs+MVs systems and not observed in cases of GUVs+POPS LUVs system. The number of docked LUVs particles on a single GUV increases with time, but no membrane invagination was detected even after 40 min of the LUVs addition (Figure S4A−C in the SI). Similarly, we examined the effect of added MVs on POPS-rich GUVs (negative ζ potential), Figure S4D−F. The MVs do not appear at the periphery of the GUVs and are preferably diffused in the solution phase. The data in Figures 1 and 2 confirm that LUVs and MVs dock onto oppositely charged GUVs via electrostatic interactions. Notably, only MVs can merge with the oppositely charged GUVs and induce membrane invagination.

Figure 2A,B shows micrographs of two representative GUVs with either single or multiple membrane invagination sites. The timestamp confocal images in Figure 2A show that the invaginated sites remain intact with the GUV (up to imaging time, i.e., 40 min). These images of single GUVs were recorded by scanning the same z-stack with minor adjustments in the focus. While the number of invagination sites increases for a few GUVs, membrane fission or tubulation events are not detected. The invaginated GUVs enlarge in diameter with time. We plotted the diameter of 5 representative DiO-labeled GUVs upon MVs addition in Figure 2C, and it shows a steady increase in the GUVs size (analysis details in the Method-ssection and Figure S5A in the SI). The size of the invaginated sites does not always increase with time. Also, the spherical shape of GUVs distorts with time and the membrane rim appears less stiff; see images Figure 2A at 40 min and Figure 2B at 30 min, indicating an increased membrane fluidity.

We analyzed the smooth fluorescence signal of DiO and DiI along the GUVs rim (one plane of GUVs). These fluorophores are a FRET pair, but the FRET signal of the mixed membrane was not detected in our experiments. The rapid membrane mixing, lateral mobility of the fluorophores, and enlargement of the GUV are reasons for weak or nondetectable FRET signal. Hence, we measured the signal of both fluorophores using the

https://doi.org/10.1021/acsomega.4c08971
ACS Omega 2024, 9, 46615−46626

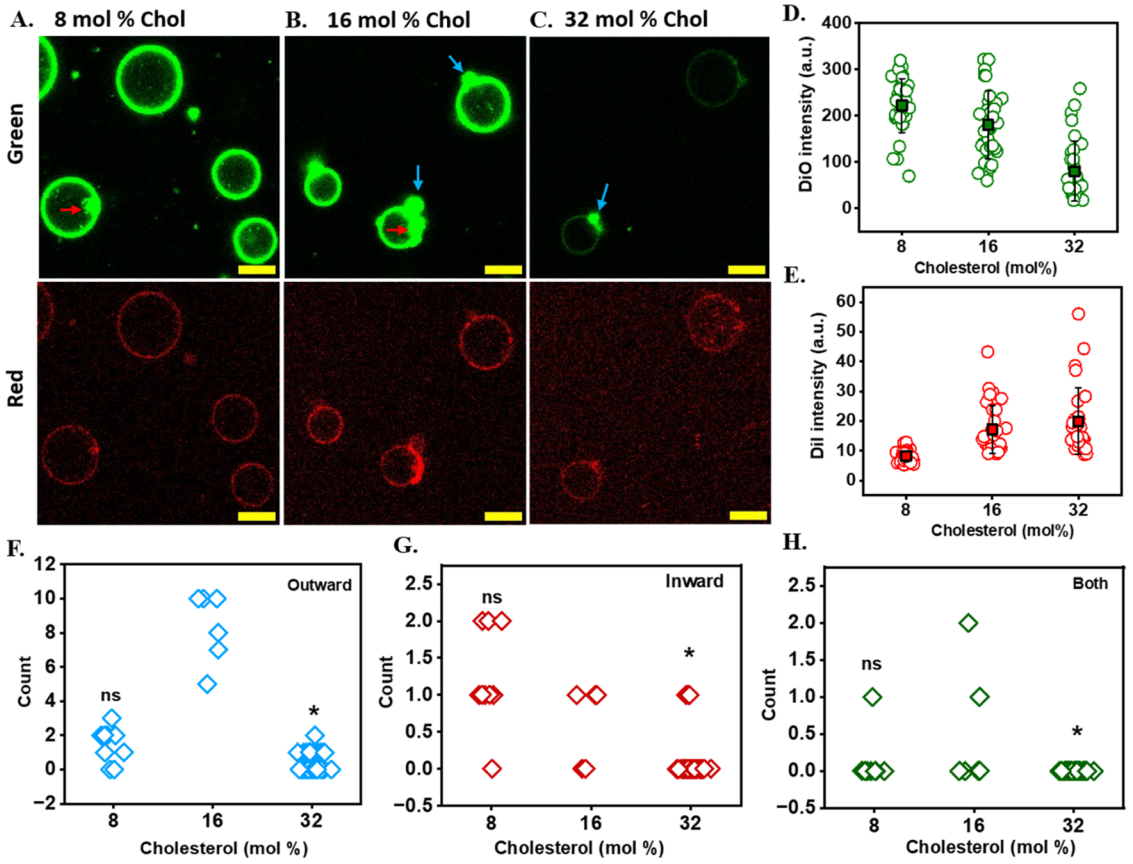

Figure 3. Membrane fusion and invaginations for GUVs with different cholesterol content. (A−C) Confocal images of 8, 16, and 32 mol % chol GUVs incubated with MVs for 10 min. Red and blue arrows indicate inward and outward invagination, respectively. Scatter plot of the mean (D) DiO intensity and (E) DiI intensity on GUV membrane (N = 33) for all three systems. Scatter plot of all three systems for (F) outward (positive curvature), (G) inward invagination (negative curvature), and (H) GUVs having both positive and negative curvature simultaneously in the same GUV. Significance of the difference from 16 mol % as reference was assessed by nonparametric Kruskal−Wallis ANOVA with Dunn's test; ns = not significant; *p < 0.01; ns = nonsignificant. Scale bar: 10 μm.

standard excitation−emission setup of the microscope. Signal statistics of 20 single GUVs are presented in Figure 2D,E (details in the Methods section and Figure S5B in the SI). The signal of the GUV membrane (DiO, green channel) fluctuates between 100 and 400 au upon MVs addition and remains similar within 10−40 min. This means that the GUVs membrane remains intact, and DiO molecules stay anchored in the membrane without much perturbation. The DiI signal on GUVs is introduced by the merged MVs, and it increases with time (Figure 2E). There are two possible explanations for this: (i) more MVs are fusing with time and (ii) dequenching of the transferred DiI in GUVs. The former is not likely to be the case, as the added MVs particles fuse with GUVs instantaneously. The signal dequenching is plausible because of the improved distribution of DiI and enlargement of the membrane of GUVs.

Next, we explored membrane merging and invagination by altering the lipid composition of GUVs. The DOTAP is essential for docking of MVs. Thereby, we focused on the effect of cholesterol and SM on membrane invagination. Cholesterol is known to influence membrane fusion of different systems such as SNARE-mediate membrane fusion in neurons, fusion of enveloped viruses on cell membranes,[35,36] etc. It prefers to partition in the liquid order (L_o) phase and influences the lipid packing, phase separation, etc. which in turn affects the membrane rigidity and line tension.[43,44] Also, the extent of cholesterol partition and resulting lipid packing depend on the type (molecular structure) and amount (mol %) of associated lipids such as SM, saturated lipids.[45] Therefore, the lateral and interleaflet distribution of cholesterol and associated lipids can introduce membrane asymmetry which is often connected with membrane deformation and invagination.[46−48] Therefore, experiments were conducted using the positively charged GUVs at different mol % of cholesterol, i.e., 8, 16, and 32 mol % and also, by omitting either cholesterol or SM in the composition (Table 1 in the Methods section). We observed that the lipid composition affects the number of produced GUVs (details in the Methodssection). Keeping this in mind, we have analyzed the same number of vesicles for all compositions.

Representative confocal images of 8, 16, and 32 mol % chol GUVs upon membrane fusion with MVs are shown in Figure 3A−C. The green channel signal is relatively lower in 32 mol % chol GUVs (Figure 3D). This is the case with or without MVs addition, indicating that DiO insertion is less efficient in 32 mol % GUVs. This high cholesterol in a lipid bilayer can increase the membrane rigidity by forming a liquid order or solid phase of the lipids. On the contrary, the DiI signal from the fused MVs is slightly greater for the 32 mol % chol GUVs (Figure 3E). Two possible explanations for this are that (i) MVs fusion is more effective for these GUVs and (ii) the number of fused MVs per single GUV is higher because of the

https://doi.org/10.1021/acsomega.4c08971
ACS Omega 2024, 9, 46615−46626

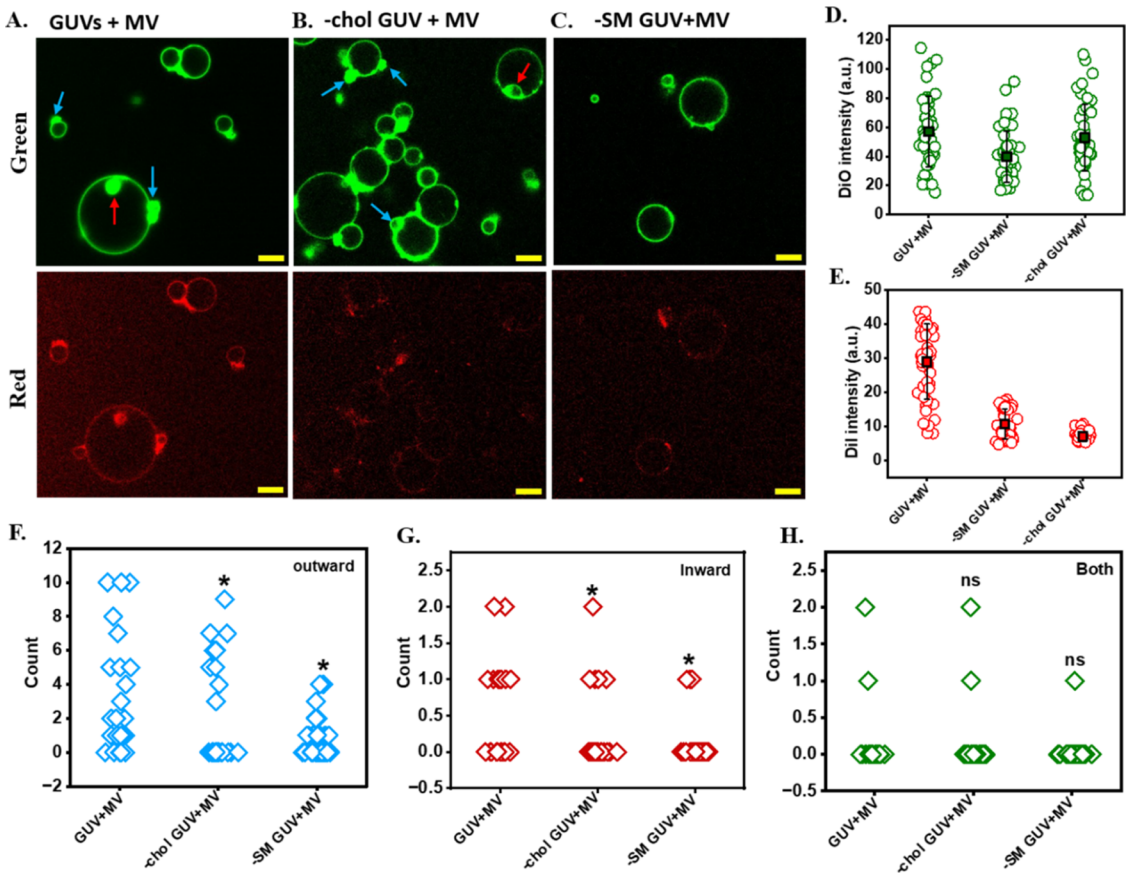

Figure 4. Membrane fusion and invaginations for GUVs without either cholesterol or SM. (A−C) Confocal Images of GUVs (composition as described in Figure 1), -chol GUVs, and -SM GUVs incubated with MVs for 10 min. Blue and red arrows indicate outward and inward invagination, respectively. Scatter plot of mean (D) DiO intensity and (E) DiI intensity on GUV membrane (N = 50) for all of the three compositions. Scatter plot of all three systems for (F) outward (positive curvature), (G) inward invagination (negative curvature), and (H) GUVs having both positive and negative curvature simultaneously in the same GUV. N = 200 GUVs of each type were analyzed in these plots (details in the Methods section). Significance of the difference from GUV+MV data as reference was assessed by nonparametric Kruskal−Wallis ANOVA with Dunn's test; *p < 0.05; ns = not significant; Scale bar: 10 μm.

low production of the GUVs (fewer vesicles within the sample chamber). The latter is likely to be the reason, and this will be clear as we discuss the data of Figure 4. We compared the number of invaginated vesicles per imaged area (224.92 × 224.92 μm^2) for these GUV types, see Figure 3F−H. Statistical analysis of the corresponding data reveals that the number of vesicles with outward invagination(s) is comparable for 8 and 16 mol % chol GUVs and it is significantly low for 32 mol % chol GUVs (Figure 3F). In general, the number of vesicles with inward and both types of invaginations are low for all three GUVs types (Figure 3G,H, respectively). About 65% of the 16 mol % chol GUVs show outward invagination. This average value is about 15% for the 32 mol % chol GUVs. Inward invagination is detected for 5−15% of these GUVs and only 1−2% of vesicles show both types of invaginations. These data reveal that our GUV compositions experience a budding-like phenomenon, as the outward invaginations are mostly seen on the membrane rim. A high cholesterol content (such as at 32 mol %) in these positively charged GUVs causes weaker membrane deformation resulting in fewer invagination sites.

Next, we examined the membrane fusion and invagination in cholesterol and SM-free vesicles, i.e., -chol GUVs and -SM GUVs, respectively (Table 1). The representative confocal micrographs in Figure 4A−C show the fluorescence signals in both channels and inward/outward invaginations of the GUVs upon interaction with MVs. Here we chose 16 mol % chol GUVs for data comparison. The DiO intensities of these GUV compositions remain similar even after membrane mixing (Figure 4D). In contrast, the DiI signal per vesicle varies significantly across different GUV compositions (Figure 4E). It

Table 1. Names and Chemical Compositions of the Formulated GUVs

GUVs name	lipid composition	mol %	molar ratio
16 mol % chol GUVs	DOPC:DOTAP:SM:Chol	32:16:32:16	2:1:2:1
32 mol % chol GUVs	DOPC:DOTAP:SM:Chol	16:16:32:32	1:1:2:2
8 mol % chol GUVs	DOPC:DOTAP:SM:Chol	40:16:32:8	2.5:1:2:0.5
DSPC GUVs	DOPC:DOTAP:DSPC:Chol	32:16:32:16	2:1:2:1
POPS GUVs	DOPC:POPS:SM:Chol	32:16:32:16	2:1:2:1
-SM GUVs	DOPC:DOTAP:Chol	46.5:23.2:23.2	2:1:1
-Chol GUVs	DOPC:DOTAP:SM	37.7:18.8:37.7	2:1:2

https://doi.org/10.1021/acsomega.4c08971
ACS Omega 2024, 9, 46615−46626

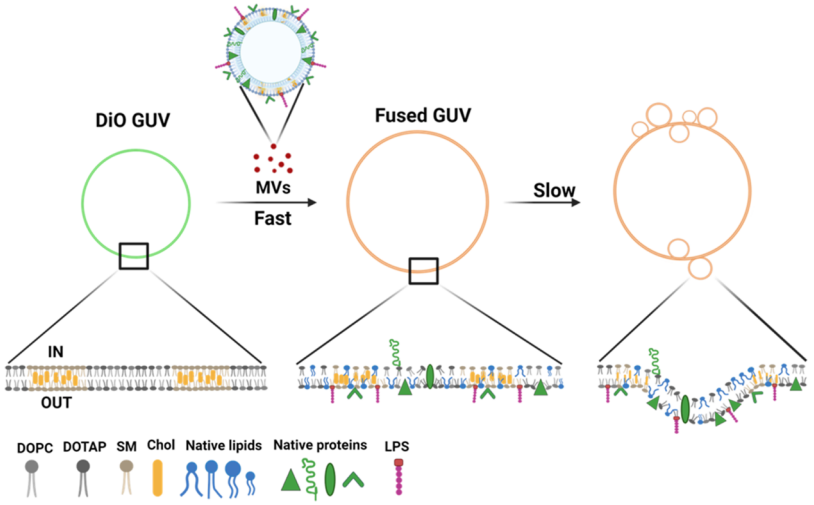

Figure 5. Plausible mechanism of membrane invagination. Scheme of membrane mixing between a GUV and MVs. The molecular changes or rearrangement generate the interleaflet (trans-bilayer) and lateral asymmetry, which in turn can affect membrane tension. The scheme depicts the resulting membrane curvature on the GUV membrane, and this appears as an outward invagination site.

is notably low for the -chol and -SM GUVs. This can be attributed to the high production rate of the -chol GUVs, as indicated by the number of vesicles detected within the imaging area (224.92 × 224.92 μm^2). Thus, the number of MV particles per vesicle (-chol GUV) is lower resulting in fewer fusion events per single GUV. Meanwhile, the production rate of -SM GUVs is comparable to that of GUVs containing 16 mol % cholesterol, as evidenced by imaging data. Therefore, the reduced DiI signal suggests that fusion between MVs and -SM GUVs is less efficient.

Membrane invagination sites are detected for -chol GUVs, whereas the sites are rare for -SM GUVs. On average, ∼50, ∼30, and ∼15% of the imaged vesicles show outward invagination for the 16 mol % chol, -chol, and -SM compositions, respectively. Inward invagination is detected for a small percentage (2−8%) of these GUVs. The invaginated sites appear only upon membrane mixing with MVs (Figure S6A in the SI). Figure 4F−H represents these data in terms of the number distribution of the GUVs with inward, outward, and both types of invaginations upon fusion with MVs. Together, Figures 3 and 4 data mean that the cholesterol is not essential for the membrane invagination of the GUVs and a high concentration of cholesterol in GUVs reduces the extent of membrane invagination of the parent GUVs. Our imaging data reveal that SM is an essential molecular factor for the membrane invagination of the formulated GUVs. The -SM GUVs have a ternary lipid composition resulting in 23 mol % cholesterol in the GUV membrane (Table 1). This increased cholesterol content in -SM GUVs may affect the data comparison in Figure 4. Therefore, we formulated GUVs by replacing SM with the DSPC lipid (both have saturated lipid tails). The DSPC GUVs with quaternary lipid composition contain 16 mol % cholesterol (Table 1). The membrane invagination data of DSPC GUVs are comparable to those of -SM GUVs (Figure S6B−H in the SI). This means that SM is an essential factor for the membrane invagination of the positively charged GUVs having cholesterol content within 0 to 32 mol % (Figures 3 and 4).

DISCUSSION

Our fluorescence imaging (single- and dual-color) and FRAP data (Figure 1) confirm that MVs isolated from mammalian cells can effectively fuse to DOTAP-rich GUVs. The membrane fusion is rapid or instantaneous, resulting in a transfer of native membrane lipids and protein to the GUVs without the requirement of any external stimuli such as pH or ions. Schmid et al. have reported a similar system to transfer native membrane components to GUVs using calcium ions as a trigger for effective membrane mixing.[23] Here, we utilize electrostatic interaction for membrane docking of negatively charged MVs on positively charged GUVs. Earlier reports by Solon et al.,[37] Lira et al.,[18] Dolder et al.,[38] and others exhibit that oppositely charged LUVs or SUVs or proteo-SUVs can fuse with the membrane of GUVs. As per these literature reports, the fusion is rapid and reported to occur within milliseconds. A major difference of our finding from these reported data is that the membrane mixing is specific to MVs and does not occur while using oppositely charged LUVs. Although the latter can dock on the DOTAP GUVs, they do not fuse. Thus, we concluded that membrane docking is triggered by the electrostatic interactions, and the fusion is activated by native membrane components. This also means that the GUV composition is critical for membrane fusion. We used a quaternary lipid mixture as GUV composition, and the reference literature used binary or tertiary lipid compositions in their experiments. This explains the observed differences in our results.

The membrane fusion between MVs and GUVs leads to an influx of native lipids and proteins in the membrane of the GUVs. The increase in the GUV diameter is in agreement with the influx. We confirm that native ACE2 is transferred to the majority of GUVs (∼80%) upon membrane mixing and extrapolate that other membrane proteins can also be transferred. We can support this argument from the kinetics of membrane mixing. The kinetics of membrane fusion mediated by proteo-liposomes containing a single type of protein (SNARE proteins) is in the minute scale[39] and the fusion gets rapid (within 10 s) only in the presence of calcium ion.[40] However, we detect an instantaneous membrane mixing of MVs to a single GUV without any calcium ion. The isolated

https://doi.org/10.1021/acsomega.4c08971
ACS Omega 2024, 9, 46615−46626

MVs are rich in proteins with fusion peptide sequences and fusogenic lipids with smaller head groups. We hypothesize that these native proteins and lipids collectively drive the fusion process.

The highly curved MVs (∼100 nm in diameter; curvature is inversely proportional to the diameter of vesicles)[41] contain ∼50% more lipids in the outer leaflet than in the inner leaflet.[42] The fusion of multiple MVs to a single GUV introduces an excess lipid in the outer leaflet of the GUV (scheme in Figure 5). Also, GUVs become rich in the transmembrane, peripheral, and lipid-anchored proteins at the fusion sites (Figure 5). Because of their relatively weak lateral mobility, these proteins introduce a lateral asymmetry in the parent GUV membrane. In these ways, the distribution of membrane components and lamellarity of the GUVs are perturbed. Membrane remodeling of the GUVs can compensate for these asymmetries.

Interestingly, there is a relatively long lag phase (>10 min) between the membrane mixing and the appearance of the invaginated sites (Figure 2). This could be because of the slow kinetics of the required membrane remodeling. Other studies exhibit a rapid (within 10−400 s) membrane invagination upon LUVs fusion to oppositely charged GUVs.[18,37] The use of pure lipid systems can explain the fast membrane remodeling in these cases. Here, the authors discuss that the influx of lipids drives the membrane invagination either by reducing the membrane tension (effective membrane tension becomes negative)[37] or redistributing the gained lipids area in the form of buds/protrusions.[18] Recently Nair et al. showed an introduction of native lipopolysaccharides reduces the bending rigidity of GUVs and the membrane can form protrusions upon osmotic stress.[17] Hence, it is likely that the influx of native membrane components into GUVs (after mixing with MVs) lowers the membrane tension. We argue that this lowered membrane tension and the generated membrane asymmetries are the causes of membrane remodeling and thereby the formation of membrane invagination sites on GUVs.

Our invagination analysis reveals that the outward invagination sites are higher for all compositions of GUVs examined in this work (Figures 3 and 4). About 15−65% of the GUVs (of different compositions) have outward invaginations. Upon membrane fusion, the chemical structure of the inserted native lipids such as acyl chain type/length, the headgroup, and the size ratio of head to tail group influences the extent and type of spontaneous curvature. The results of Nair et al. show that the native lipopolysaccharides (LPS) favor spontaneous budding (outward protrusion) from the membrane of GUVs.[17] Also, the inner leaflet of the plasma membrane,[43] and thus the isolated MVs, are rich in PE lipids, which prefer nonlamellar structures.[44] The endogenous PE lipids and LPS transferred to GUVs may favor outward membrane invaginations (scheme of Figure 5). The shallow insertion of peripheral proteins and the complexation/association of lipids with the transmembrane sites of proteins perturb the local lamellar structure of lipids and can be compensated by outward membrane bending[45,46] (Figure 5).

Among the different lipid compositions studied in this work, GUVs with 16 mol % cholesterol and 32 mol % of sphingomyelin (SM) show the highest number of outward invaginations. Explaining the role of cholesterol and SM in membrane fusion and invagination is not straightforward because we used complex (ternary/quaternary) lipid mixtures for GUVs formation. Although the GUV compositions can be controlled accurately (as confirmed from ζ potential measurements) and the GUVs are in the liquid-disorder phase, we cannot distinguish the extent of their lateral (microscopic) and trans-bilayer lipid asymmetry. The inherent membrane asymmetry of the GUVs can catalyze or accelerate the formation of invaginated sites upon fusion. We found that SM lipid is essential for the membrane fusion and invagination (Figure 4). Contrary to some reports on membrane fusion for viruses,[36,47,48] LUVs,[49,50] we observed that cholesterol that affects membrane rigidity/line tension[51,52] is not critical for MVs fusion to GUVs and thereby, for the membrane invaginations (Figure 3). A high cholesterol content (such as 32 mol %) in the GUVs disfavors membrane invaginations, likely because of increased rigidity of the GUV bilayer.

Beyond the GUVs-MVs system studied in this work, membrane fusion and invagination have a broader aspect or roles in cellular processes. Both processes are essential in intra- and intercellular transport. Fusion is well known for chemical transport for neuronal signaling,[53] in delivery of viral genome,[54] endosomal delivery,[55] etc. On the other hand, membrane invagination is the process for generating vesicular vehicles such as endosomes, exosomes, buds, etc. which mediate cellular transport. Typically, molecular triggers such as protein binding or insertion induce membrane bending (change in curvature) which matures into a spherical bud (inward or outward).[41,56] The energy required for the formation of a single spherical vesicle from a flat lipid bilayer is 250−650 k_BT. This high energy cost necessitates the engagement of multiple proteins, lipid machinery, cooperative interactions, and synergistic processes for membrane invagination. These arguments are valid and well reflected in our data.[41,56,57] For example, the specificity of fusion by MVs (not by LUVs) and the rapid membrane mixing confirm that multiple proteins and lipids are engaged in the process; thus, cooperative or synergistic interactions are in action. The lag phase of the membrane invagination is the sign of membrane remodeling initiated upon the generated membrane asymmetry (later and trans-bilayer) and altered membrane tension. The role of lipid machinery is validated as we confirm that the SM lipid in GUVs is essential for membrane invagination.

In conclusion, we have established an effective method for transferring native lipids and proteins to positively charged GUVs without external stimuli, such as pH or calcium ions. The GUVs reconstituted with native membrane components behave as model cells exhibiting membrane invaginations that are essential for cellular transport.

MATERIALS AND METHODS

Materials. *N*-Ethylmaleimide (NEM) and 4-(2-hydroxyethyl)-1-piperazineethanesulfonic acid (HEPES) buffer were brought from SRL (Sisco research laboratory), India. Liss Rhod PE {1,2-dioleoyl-*sn*-glycero-3-phosphoethanolamine-*N*-(lissamine rhodamine B sulfonyl)}, DiO (3,3′-dioctadecyloxacarbocyanine Perchlorate), and DiI (1,1′-Dioctadecyl-3,3,3′,3′-Tetramethylindocarbocyanine Perchlorate) were obtained from Sigma-Aldrich. ACE2 recombinant rabbit monoclonal antibody, Goat antirabbit IgG (H+L) cross-adsorbed secondary antibody (Alexa Fluor 488), Dulbecco's modified Eagle's medium (DMEM, L-glutamine, sodium pyruvate, high D-glucose; Gibco), Trypsin-EDTA (0.05−0.02% (w/v), Gibco), 1% penicillin-streptomycin (PenStrep, 100 units/mL; Gibco), fetal bovine serum (FBS; Gibco), T25 cm^2 cell culture flask, and polyvinyl alcohol (M.W.146−186

https://doi.org/10.1021/acsomega.4c08971
ACS Omega 2024, 9, 46615−46626

kDa, 99.3−100% hydrolyzed) were from Thermo Fisher Scientific, India. POPC (1-palmitoyl-2-oleoyl-*sn*-glycero-3-phosphocholine, cat. no.850457), DOPC (1,2-dioleoyl-*sn*-glycero-3-phosphocholine, cat. no. 850375), cholesterol (cat. no. 700000), Brain Sphingomyelin (cat. no. 860062), DOTAP (1,2-dioleoyl-3-trimethylammonium-propane, cat. no. 890890), and POPS (1-palmitoyl-2-oleoyl-*sn*-glycero-3-phospho-L-serine, cat. no. 840034) were purchased from Avanti Polar Lipids in white lyophilized powder form. Potassium dihydrogen orthophosphate disodium hydrogen phosphate, sodium chloride (NaCl), calcium chloride ($CaCl_2$), and potassium chloride were purchased from Finar, India. Borosilicate cover glass (22 mm × 50 mm; 22 mm × 22 mm) was from VWR (Avantor). Sodium dodecyl sulfate (SDS) was obtained from SD Fine Chem Limited (India). Sylgard 184 silicone polydimethylsiloxane (PDMS) elastomer base and Sylgard 184 silicone elastomer curing agent or cross-linker (dimethyl methyl hydrogen siloxane copolymer) were brought from Robert McKeown Company; Branchburg, NJ.

GUV Formation. GUVs were formed by a PVA-gel-assisted hydration method. Briefly, 5% (w/v) PVA was dissolved in 280 mM sucrose solution by heating on a hot plate at 90 °C with constant stirring using a magnetic bead until the solution becomes clear. Using a pipette, 100−200 μL of this PVA solution was evenly spread on an SDS cleaned 22 mm square cover glass and kept in an oven at 80 °C for 30 min. After that, positively charged GUVs were formed by making 10−20 μL of lipid mixture containing DOPC, SM, cholesterol, and DOTAP in a 2:2:1:1 molar ratio in chloroform from 1 mg/mL stock solutions. Negatively charged GUVs were formed by adding POPS to the above mixture, instead of DOTAP.

For fluorescence imaging, 4 mol % DiO was added to the lipid mixture. This high concentration of DiO was required for the fluorescence imaging of the vesicles, attaining an adequate signal. The incorporation of DiO in membranes depends on acyl chain unsaturation of lipids, acyl chain length, charge on the headgroup, and cholesterol content.[58] These factors determine the faint or bright signal on the GUV membranes. High mol % of DiO is likely to cause artifacts in the membranes like perturbations in phospholipid packing of GUVs membrane due to headgroup-headgroup repulsions between GUVs lipids and DiO headgroup. But for GUV-Antibody binding experiments, GUVs were formed by adding 0.1 mol % DiI and the rest of the lipid composition was the same. This lipid mix was spread on the dried PVA film and kept in a vacuum for 2 h. GUVs were grown by adding 300 μL of a growing buffer of high salt concentrations (10 mM $CaCl_2$, 10 mM HEPES,150 mM NaCl) as it was found that with high-calcium-concentration GUVs were more stable and bigger in size. It is to be noted that POPS GUVs were grown by adding PBS instead of calcium buffer to avoid aggregation. Later, GUVs were incubated for 1 h at 37 °C in the dark. Before isolation, GUVs were sonicated for 1 s for the maximum detachment from the gel to the solution. Finally, GUVs were harvested by gentle pipetting and kept at 4 °C prior to the experiments. Different types of GUVs with their lipid composition are listed in Table 1.

Formation of MVs. DiI-labeled MVs were prepared by extruding isolated GPMVs supernatant 21 times through a 100 nm pore size polycarbonate membrane filter using a miniextruder (Avanti Polar Lipids). Details of cell culture and GPMV isolation in the SI.

LUVs Preparation. Negatively charged POPS LUVs with the composition POPC/POPS/DiI in 1:0.98:0.02 molar ratio (50:49:1 mol %) were formed by the thin film hydration method followed by extrusion. Details are given in the experimental section of the SI.

GUV-MVs Mixing Assay. For dual-color GUVs-MVs fusion experiments, 5 μL of DiI-labeled MVs were diluted 4 times to the buffer containing 10 mM $CaCl_2$, 10 mM HEPES, and 150 mM NaCl. The same buffer is used for GUVs formation/growth, avoiding any osmotic shock upon mixing. Later, 20 μL of DiO-labeled GUVs were added to the wells, followed by 10 min incubation with MVs. Confocal images were recorded in TRITC and FITC at an interval of 10 min. For single-color experiments, the same assay was followed with unlabeled GUVs and DiI-labeled GPMVs. Images were recorded in bright-field and TRITC channels in a sequential manner.

GUVs-LUVs Mixing Assay. For the GUVs-POPS LUVs or GUVs-DiI DOPC LUVs or GUVs-Rh DOPC LUVs fusion experiment, LUVs were diluted in 10 mM calcium-containing buffer to make the final concentration of 0.01 mg/mL. Later, 20 μL of GUVs were incubated with 20 μL of LUVs (0.01 mg/mL) for 10 min. Further, confocal images were recorded in FITC and TRITC filters in a sequential and time-dependent manner.

Immunofluorescence Imaging with ACE2 Antibody. Immunofluorescence experiments were performed with 20 nM (2.5 μg/mL) Goat antirabbit IgG (H+L) cross-adsorbed Alexa Fluor 488 conjugated secondary antibody. For dual-color confocal imaging, fusion between DiI-labeled GUVs and unlabeled MVs was performed as described earlier for ACE2 protein transfer. Afterward, GUVs were first incubated with 20 nM primary Rabbit monoclonal ACE2 antibody for 20 min followed by incubation with fluorescent secondary antibody for another 20 min. PBS washing was done gently 2 to 3 times to remove excess fluorophore. Images were recorded in both TRITC and FITC filter cubes. Same immunofluorescence assay was followed for experiments with unlabeled GUVs. Images were recorded in bright-field and FITC cube.

Confocal Imaging of GUVs. GUVs were imaged using homemade PDMS chambers (volume ∼50 μL) on SDS cleaned borosilicate cover glasses with 22 × 50 mm thickness. To inhibit the surface rupturing of the vesicles, the cover glass was passivated with a supported lipid bilayer made of DOPC lipid (0.1 mg/mL). Surface-settled GUVs become mobile immediately after the addition of a solution of MVs. This limited us to image the GUVs only after 10 min from the addition of MVs within which GUVs again settle on the surface and time-trace imaging of single GUVs becomes possible. Therefore, we imaged the GUVs after MVs addition for 10 min and traced the single GUVs for up to 40 min.

Confocal images of all dual-color GUVs-MVs, GUVs-LUVs and GUVs-antibody binding experiments were obtained by a Carl Zeiss GmbH (LSM780NLO) confocal microscope with 63x oil immersion objective (NA = 1.4) over a region of Interest (ROI) of 1024 × 1024 pixels or 224.92 μm × 224.92 μm where each pixel square is of 0.22 μm. GUVs and MVs were visualized through GFP (green) and Rhodamine (red) specific filters, respectively. DiO-labeled GUVs and DiI-labeled MVs samples were excited with 488 nm (Argon ion,70% of 25 mW) and 561 nm (solid state, 75% of 20 mW) laser lines (LASOS, laser manufacturer). *Z*-stacks were recorded, ensuring comprehensive coverage of GUVs by positioning

https://doi.org/10.1021/acsomega.4c08971
ACS Omega 2024, 9, 46615−46626

the lowest plane marginally above the surface, while the highest plane was adjusted to encompass the maximum extent of GUVs until defocusing occurred. Each *z*-stack (16 Bits per pixel) comprised seven slices, with a step size of 1.57 μm, culminating in a total depth of 11 μm. Images or videos were analyzed using ImageJ software (ImageJ 1.53k, Java 1.8.0_172 (64-bit), NIH Maryland). (Details of epifluorescence imaging in SI)

Around 180 GUVs were analyzed in GUV-MV system where we observed that 80% of GUVs showed the smooth signal along the membrane rim. For anti-ACE2 signal analysis, we have analyzed around 60 GUVs. For this case, the number of analyzed GUVs is limited as we have also done PBS washing (2−3 times) to remove the excess fluorophore, which results in loss of GUVs with every wash.

Size Analysis of GUVs and Invagination. For size analysis of GUVs, a straight line from the diameter of GUVs was drawn such that it connects both the ends of GUVs, then by using "measure" feature we recorded the diameter (Figure S5B). The same line was fixed as ROI and size measurement was repeated at all of the time points. The size of the invagination sites protruding out from GUVs was also measured in a similar way. A total of ∼56 buds (both inward and outward included) were analyzed for size. All of the size data was collected and plotted using origin.

GUVs Count for Membrane Invagination Analysis. Invaginated GUVs were counted from each image having an area of 224.92 × 224.92 μm^2. The number of images that we analyzed was different for each composition depending on the population of GUVs in an area. For example, GUVs number per area for 8, 16, and 32 mol % were 2−25, 3−17, and 1−3, respectively. Despite of different number of analyzed images for these three systems, the total number of analyzed vesicles (N = 78) was kept the same. For -Chol GUVs and -SM GUVs, imaged vesicles were highest and lowest i.e., 20−30 and 1−4 vesicles per area, respectively. The total number of analyzed vesicles (N = 200) was the same. Data comparison of these GUVs systems was done such that we analyzed the membrane fusion and invagination events for the same number of vesicles of each type. We have analyzed invagination sites which are in the size range of 2−4 μm arising from the parent GUVs having a diameter of 10−20 μm. All of the collected data was plotted as "scatter interval" and then assessed by nonparametric Kruskal−Wallis ANOVA with Dunn's test.

Percentage Calculation of Invaginated GUVs. Percent number for the GUVs with inward invaginations, outward invaginations, or both was calculated with the above-collected data only using the below calculation:

$$\%\ \text{of invaginated GUVs} = \frac{\text{total no. of (inward/outward/both) invaginated GUVs}}{\text{total number of analysed GUVs}} \times 100$$

Intensity Analysis of GUVs. For intensity analysis, we selected the square box from the polygon tool of ImageJ and then fixed an ROI for covering a single GUV within that square box as shown in Figure S5C in the SI. The same ROI was used for red channel and consecutive time-dependent images as well. From the "measure" feature, we got the mean intensity of the ROI. In this manner, we recorded the intensity of several GUVs in both green and red channels. All of the mean intensity data was plotted in "scatter interval plot" using Origin.

■ ASSOCIATED CONTENT

Supporting Information

The Supporting Information is available free of charge at https://pubs.acs.org/doi/10.1021/acsomega.4c08971.

Experimental section dealing with Cell culture, GPMV isolation, preparation of LUVs, ζ potential, and size measurement; determination of endogenous ACE2 using WB, epifluorescence imaging, and analyzed data (PDF)

Confocal images (*z*-stacks) for GUVs+MVs systems at different mol % of cholesterol (AVI)

■ AUTHOR INFORMATION

Corresponding Author

Nagma Parveen − *Department of Chemistry, Indian Institute of Technology Kanpur, 208016 Kanpur, India;* orcid.org/0000-0003-4577-7721; Email: nagma@iitk.ac.in

Authors

Garvita Dhanawat − *Department of Chemistry, Indian Institute of Technology Kanpur, 208016 Kanpur, India*

Manorama Dey − *Department of Chemistry, Indian Institute of Technology Kanpur, 208016 Kanpur, India*

Anirudh Singh − *Department of Chemistry, Indian Institute of Technology Kanpur, 208016 Kanpur, India*

Complete contact information is available at: https://pubs.acs.org/10.1021/acsomega.4c08971

Author Contributions

The manuscript was written with the contributions of all authors. All authors have approved the final version of the manuscript.

Notes

The authors declare no competing financial interest.

■ ACKNOWLEDGMENTS

This work was supported by the Science and Engineering Research Board, India (CRG/2023/002612). Garvita Dhanawat thanks the Council of Scientific and Industrial Research, India, for the fellowship.

■ REFERENCES

(1) Reeves, J. P.; Dowben, R. M. Formation and Properties of Thin-walled Phospholipid Vesicles. *J. Cell. Physiol.* **1969**, *73* (1), 49−60.

(2) Tehran, D. A.; López-Hernández, T.; Maritzen, T. Endocytic Adaptor Proteins in Health and Disease: Lessons from Model Organisms and Human Mutations. *Cells* **2019**, *8* (11), 1−52.

(3) Barrow, E.; Nicola, A. V.; Liu, J. Multiscale Perspectives of Virus Entry via Endocytosis. *Virol. J.* **2013**, *10* (177), 1−11.

(4) Alabi, A. A.; Tsien, R. W. Perspectives on Kiss-and-Run: Role in Exocytosis, Endocytosis, and Neurotransmission. *Annu. Rev. Physiol.* **2013**, *75*, 393−422.

(5) Chiang, H. C.; Shin, W.; Zhao, W. D.; Hamid, E.; Sheng, J.; Baydyuk, M.; Wen, P. J.; Jin, A.; Momboisse, F.; Wu, L. G. Post-Fusion Structural Changes and Their Roles in Exocytosis and Endocytosis of Dense-Core Vesicles. *Nat. Commun.* **2014**, *5*, No. 3356, DOI: 10.1038/ncomms4356.

(6) Kahya, N.; Pécheur, E. I.; De Boeij, W. P.; Wiersma, D. A.; Hoekstra, D. Reconstitution of Membrane Proteins into Giant

Unilamellar Vesicles via Peptide-Induced Fusion. *Biophys. J.* **2001**, *81* (3), 1464−1474.
(7) Agudo-Canalejo, J.; Lipowsky, R. Critical Particle Sizes for the Engulfment of Nanoparticles by Membranes and Vesicles with Bilayer Asymmetry. *ACS Nano* **2015**, *9* (4), 3704−3720.
(8) Praper, T.; Sonnen, A. F. P.; Kladnik, A.; Andrighetti, A. O.; Viero, G.; Morris, K. J.; Volpi, E.; Lunelli, L.; Serra, M. D.; Froelich, C. J.; Gilbert, R. J. C.; Anderluh, G. Perforin Activity at Membranes Leads to Invaginations and Vesicle Formation. *Proc. Natl. Acad. Sci. U.S.A.* **2011**, *108* (52), 21016−21021.
(9) Lipowsky, R. Coupling of Bending and Stretching Deformations in Vesicle Membranes. *Adv. Colloid Interface Sci.* **2014**, *208*, 14−24.
(10) Zhou, Q.; Peng, Y. X.; Wang, P.; Jiang, Z. Y.; Zhao, X. J.; Zhu, T. Membrane Inward/Outward Budding and Transition Pathway Induced by the Asymmetric Solutions. *Colloids Surf., A* **2023**, *675* (May), No. 132111.
(11) Baumgart, T.; Hess, S.; Webb, W. Imaging Coexisting Fluid Domains in Biomembrane Models Coupling Curvature and Line Tension. *Nature* **2003**, *425* (October), 821−824.
(12) Bacia, K.; Schwille, P.; Kurzchalia, T. Sterol Structure Determines the Separation of Phases and the Curvature of the Liquid-Ordered Phase in Model Membranes. *Proc. Natl. Acad. Sci. U.S.A.* **2005**, *102* (9), 3272−3277.
(13) Nomura, F.; Inaba, T.; Ishikawa, S.; Nagata, M.; Takahashi, S.; Hotani, H.; Takiguch, K. Microscopic Observations Reveal That Fusogenic Peptides Induce Liposome Shrinkage Prior to Membrane Fusion. *Proc. Natl. Acad. Sci. U.S.A.* **2004**, *101* (10), 3420−3425.
(14) Yu, Y.; Vroman, J. A.; Bae, S. C.; Granick, S. Vesicle Budding Induced by a Pore-Forming Peptide. *J. Am. Chem. Soc.* **2010**, *132* (1), 195−201.
(15) Schubert, T.; Römer, W. How Synthetic Membrane Systems Contribute to the Understanding of Lipid-Driven Endocytosis. *Biochim. Biophys. Acta - Mol. Cell Res.* **2015**, *1853* (11), 2992−3005.
(16) Rydell, G. E.; Svensson, L.; Larson, G.; Johannes, L.; Römer, W. Human GII.4 Norovirus VLP Induces Membrane Invaginations on Giant Unilamellar Vesicles Containing Secretor Gene Dependent A1,2-Fucosylated Glycosphingolipids. *Biochim. Biophys. Acta, Biomembr.* **2013**, *1828* (8), 1840−1845.
(17) Nair, K. S.; Raj, N. B.; Nampoothiri, K. M.; Mohanan, G.; Acosta-Gutiérrez, S.; Bajaj, H. Curved Membrane Structures Induced by Native Lipids in Giant Vesicles. *J. Colloid Interface Sci.* **2022**, *611*, 397−407.
(18) Lira, R. B.; Robinson, T.; Dimova, R.; Riske, K. A. Highly Efficient Protein-Free Membrane Fusion: A Giant Vesicle Study. *Biophys. J.* **2019**, *116* (1), 79−91.
(19) Litschel, T.; Schwille, P. Protein Reconstitution Inside Giant Unilamellar Vesicles. *Annu. Rev. Biophys.* **2021**, *50* (May), 525−548.
(20) Jørgensen, I. L.; Kemmer, G. C.; Pomorski, T. G. Membrane Protein Reconstitution into Giant Unilamellar Vesicles: A Review on Current Techniques. *Eur. Biophys. J.* **2017**, *46* (2), 103−119.
(21) Motta, I.; Gohlke, A.; Adrien, V.; Li, F.; Gardavot, H.; Rothman, J. E.; Pincet, F. Formation of Giant Unilamellar Proteo-Liposomes by Osmotic Shock. *Langmuir* **2015**, *31* (25), 7091−7099.
(22) Horger, K. S.; Liu, H.; Rao, D. K.; Shukla, S.; Sept, D.; Ambudkar, S. V.; Mayer, M. Hydrogel-Assisted Functional Reconstitution of Human P-Glycoprotein (ABCB1) in Giant Liposomes. *Biochim. Biophys. Acta, Biomembr.* **2015**, *1848* (2), 643−653.
(23) Schmid, Y. R. F.; Scheller, L.; Buchmann, S.; Dittrich, P. S. Calcium-Mediated Liposome Fusion to Engineer Giant Lipid Vesicles with Cytosolic Proteins and Reconstituted Mammalian Proteins. *Adv. Biosyst.* **2020**, *4* (11), No. e2000153.
(24) Weinberger, A.; Tsai, F. C.; Koenderink, G. H.; Schmidt, T. F.; Itri, R.; Meier, W.; Schmatko, T.; Schröder, A.; Marques, C. Gel-Assisted Formation of Giant Unilamellar Vesicles. *Biophys. J.* **2013**, *105* (1), 154−164.
(25) Moreno-Pescador, G.; Arastoo, M. R.; Ruhoff, V. T.; Chiantia, S.; Daniels, R.; Bendix, P. M. Thermoplasmonic Vesicle Fusion Reveals Membrane Phase Segregation of Influenza Spike Proteins. *Nano Lett.* **2023**, *23* (8), 3377−3384.
(26) Souissi, M.; Pernier, J.; Rossier, O.; Giannone, G.; Le Clainche, C.; Helfer, E.; Sengupta, K. Integrin-Functionalised Giant Unilamellar Vesicles via Gel-Assisted Formation: Good Practices and Pitfalls. *Int. J. Mol. Sci.* **2021**, *22* (12), No. 6335.
(27) Baumgart, T.; Hunt, G.; Farkas, E. R.; Webb, W. W.; Feigenson, G. W. Fluorescence Probe Partitioning between Lo/Ld Phases in Lipid Membranes. *Biochim. Biophys. Acta, Biomembr.* **2007**, *1768* (9), 2182−2194.
(28) Sych, T.; Gurdap, C. O.; Wedemann, L.; Sezgin, E. How Does Liquid-liquid Phase Separation in Model Membranes Reflect Cell Membrane Heterogeneity? *Membranes* **2021**, *11* (5), No. 323, DOI: 10.3390/membranes11050323.
(29) Sezgin, E.; Kaiser, H. J.; Baumgart, T.; Schwille, P.; Simons, K.; Levental, I. Elucidating Membrane Structure and Protein Behavior Using Giant Plasma Membrane Vesicles. *Nat. Protoc.* **2012**, *7* (6), 1042−1051.
(30) Dey, M.; Dhanawat, G.; Gupta, D.; Goel, A.; Harshan, K. H.; Parveen, N. Giant Plasma Membrane Vesicles as Cellular-Mimics for Probing SARS-CoV-2 Binding at Single Particle Level. *ChemistrySelect* **2023**, *8* (33), 1−11.
(31) Liu, H. Y.; Grant, H.; Hsu, H. L.; Sorkin, R.; Bošković, F.; Wuite, G.; Daniel, S. Supported Planar Mammalian Membranes as Models of in Vivo Cell Surface Architectures. *ACS Appl. Mater. Interfaces* **2017**, *9* (41), 35526−35538.
(32) György, B.; Szabó, T. G.; Pásztói, M.; Pál, Z.; Misják, P.; Aradi, B.; László, V.; Pállinger, É.; Pap, E.; Kittel, Á.; Nagy, G.; Falus, A.; Buzás, E. I. Membrane Vesicles, Current State-of-the-Art: Emerging Role of Extracellular Vesicles. *Cell. Mol. Life Sci.* **2011**, *68* (16), 2667−2688.
(33) Fossati, M.; Goud, B.; Borgese, N.; Manneville, J.-B. An Investigation of the Effect of Membrane Curvature on Transmembrane-Domain Dependent Protein Sorting in Lipid Bilayers. *Cell. Logist.* **2014**, *4* (2), No. e29087.
(34) Syga, Ł.; Spakman, D.; Punter, C. M.; Poolman, B. Method for Immobilization of Living and Synthetic Cells for High-Resolution Imaging and Single-Particle Tracking. *Sci. Rep.* **2018**, *8* (1), No. 13789.
(35) Chang, J.; Kim, S. A.; Lu, X.; Su, Z.; Seong, K. K.; Shin, Y. K. Fusion Step-Specific Influence of Cholesterol on SNARE-Mediated Membrane Fusion. *Biophys. J.* **2009**, *96* (5), 1839−1846.
(36) Yang, S. T.; Kreutzberger, A. J. B.; Lee, J.; Kiessling, V.; Tamm, L. K. The Role of Cholesterol in Membrane Fusion. *Chem. Phys. Lipids* **2016**, *199*, 136−143.
(37) Solon, J.; Pécréaux, J.; Girard, P.; Fauré, M. C.; Prost, J.; Bassereau, P. Negative Tension Induced by Lipid Uptake. *Phys. Rev. Lett.* **2006**, *97* (9), No. 098103.
(38) Dolder, N.; Müller, P.; von Ballmoos, C. Experimental Platform for the Functional Investigation of Membrane Proteins in Giant Unilamellar Vesicles. *Soft Matter* **2022**, *18* (31), 5877−5893.
(39) Weber, T.; Zemelman, B. V.; McNew, J. A.; Westermann, B.; Gmachl, M.; Parlati, F.; Söllner, T. H.; Rothman, J. E. SNAREpins: Minimal Machinery for Membrane Fusion. *Cell* **1998**, *92* (6), 759−772.
(40) Kyoung, M.; Srivastava, A.; Zhang, Y.; Diao, J.; Vrljic, M.; Grob, P.; Nogales, E.; Chu, S.; Brunger, A. T. In Vitro System Capable of Differentiating Fast Ca 2+-Triggered Content Mixing from Lipid Exchange for Mechanistic Studies of Neurotransmitter Release. *Proc. Natl. Acad. Sci. U.S.A.* **2011**, *108* (29), E304−E313, DOI: 10.1073/pnas.1107900108.
(41) Cail, R. C.; Drubin, D. G. Membrane Curvature as a Signal to Ensure Robustness of Diverse Cellular Processes. *Trends Cell Biol.* **2023**, *33* (5), 427−441.
(42) McMahon, H. T.; Gallop, J. L. Membrane Curvature and Mechanisms of Dynamic Cell Membrane Remodelling. *Nature* **2005**, *438*, 590−596.
(43) Ingólfsson, H. I.; Melo, M. N.; Van Eerden, F. J.; Arnarez, C.; Lopez, C. A.; Wassenaar, T. A.; Periole, X.; De Vries, A. H.; Tieleman, D. P.; Marrink, S. J. Lipid Organization of the Plasma Membrane. *J. Am. Chem. Soc.* **2014**, *136* (41), 14554−14559.

https://doi.org/10.1021/acsomega.4c08971
ACS Omega 2024, 9, 46615−46626

(44) Yang, P. L. Metabolomics and Lipidomics: Yet More Ways Your Health Is Influenced by Fat. *Viral Pathog.* **2016**, No. January, 181−198.
(45) Frolov, V. A.; Shnyrova, A. V.; Zimmerberg, J. Lipid Polymorphisms and Membrane Shape. *Cold Spring Harbor Perspect. Biol.* **2011**, *3* (11), No. a004747.
(46) Marsh, D. Protein Modulation of Lipids, and Vice-Versa, in Membranes. *Biochim. Biophys. Acta, Biomembr.* **2008**, *1778*, 1545−1575.
(47) Yang, S. T.; Kiessling, V.; A Simmons, J.; M White, J.; Tamm, L. HIV Gp41-Mediated Membrane Fusion Occurs at Edges of Cholesterol-Rich Lipid Domains. *Nat. Chem. Biol.* **2015**, *11* (6), 424−431.
(48) Yang, S. T.; Kiessling, V.; Tamm, L. K. Line Tension at Lipid Phase Boundaries as Driving Force for HIV Fusion Peptide-Mediated Fusion. *Nat. Commun.* **2016**, *7*, No. 11401.
(49) Tarnok, M. E.; Guzmán, F.; Aguilar, L. F. Effects of Cholesterol on Lipid Vesicle Fusion Mediated by Infectious Salmon Anaemia Virus Fusion Peptides. *Colloids Surf., B* **2022**, *217* (June), No. 112684.
(50) Kumar, S.; Kaur, N.; Hitaishi, P.; Ghosh, S. K.; Mithu, V. S.; Scheidt, H. A. Role of Cholesterol in Interaction of Ionic Liquids with Model Lipid Membranes and Associated Permeability. *J. Phys. Chem. B* **2024**, *128* (22), 5407−5418.
(51) Epand, R. M. Proteins and Cholesterol-Rich Domains. *Biochim. Biophys. Acta, Biomembr.* **2008**, *1778* (7−8), 1576−1582.
(52) Shrivastava, S.; Paila, Y. D.; Chattopadhyay, A. Role of Cholesterol and Its Biosynthetic Precursors on Membrane Organization and Dynamics: A Fluorescence Approach. *J. Membr. Biol.* **2023**, *256* (2), 189−197.
(53) Chang, C. W.; Chiang, C. W.; Jackson, M. B. Fusion Pores and Their Control of Neurotransmitter and Hormone Release. *J. Gen. Physiol.* **2017**, *149* (3), 301−322.
(54) White, J. M.; Ward, A. E.; Odongo, L.; Tamm, L. K. Viral Membrane Fusion: A Dance Between Proteins and Lipids. *Annu. Rev. Virol.* **2023**, *10* (1), 139−161.
(55) Bright, N. A.; J Gratian, M.; Luzio, J. P. Endocytic Delivery to Lysosomes Mediated by Concurrent Fusion and Kissing Events in Living Cells. *Curr. Biol.* **2005**, *15*, 360−365.
(56) Sambre, P. D.; Ho, J. C. S.; Parikh, A. N. Intravesicular Solute Delivery and Surface Area Regulation in Giant Unilamellar Vesicles Driven by Cycles of Osmotic Stresses. *J. Am. Chem. Soc.* **2024**, *146* (5), 3250−3261.
(57) Stachowiak, J. C.; M Brodsky, F.; A Miller, E. A Cost-Benefit Analysis of the Physical Mechanisms of Membrane Curvature. *Nat. Cell Biol.* **2013**, *15* (9), 1019−1027.
(58) Lubart, Q.; Hannestad, J. K.; Pace, H.; Fjällborg, D.; Westerlund, F.; Esbjörner, E. K.; Bally, M. Lipid Vesicle Composition Influences the Incorporation and Fluorescence Properties of the Lipophilic Sulphonated Carbocyanine Dye SP-DiO. *Phys. Chem. Chem. Phys.* **2020**, *22* (16), 8781−8790.

https://doi.org/10.1021/acsomega.4c08971
ACS Omega 2024, 9, 46615−46626